Superconductivity in the medium-entropy alloys: Nb_2TiW and Nb_2TiMo

Kuan Li(李宽)[a,#], Cui-Qun Chen(陈翠群)[b,#], Lingyong Zeng(曾令勇)[a], Longfu Li(李龙夫)[a], Rui Chen(陈睿)[a], Peifeng Yu(余沛峰)[a], Kangwang Wang(王康旺)[a], Zaichen Xiang(项载琛)[a], Dao-Xin Yao(姚道新)[b,c,d,*], Huixia Luo(罗惠霞)[a, c,d,*]

[a] School of Materials Science and Engineering, Sun Yat-sen University, No. 135, Xingang Xi Road, Guangzhou, 510275, P. R. China
[b] School of Physics, Sun Yat-sen University, No. 135, Xingang Xi Road, Guangzhou, 510275, P. R. China
[c] State Key Laboratory of Optoelectronic Materials and Technologies, Sun Yat-sen University, No. 135, Xingang Xi Road, Guangzhou, 510275, P. R. China
[d] Guangdong Provincial Key Laboratory of Magnetoelectric Physics and Devices, Sun Yat-sen University, No. 135, Xingang Xi Road, Guangzhou, 510275, P. R. China

This work is supported by the National Natural Science Foundation of China (12274471, 11922415, 92165204), Guangdong Basic and Applied Basic Research Foundation (2022A1515011168), Guangzhou Basic and Applied Basic Research Project Navigation Project (2024A04J6415). The experiments and calculations reported were conducted at the Guangdong Provincial Key Laboratory of Magnetoelectric Physics and Devices, No. 2022B1212010008. Lingyong Zeng was thankful for the Postdoctoral Fellowship Program of CPSF (GZC20233299) and Fundamental Research Funds for the Central Universities, Sun Yat-sen University (29000-31610058).

[#] K. Li and C. Chen contributed equally to this work.
*Corresponding author/authors complete details (Telephone; E-mail:) (+86)-2039386124, E-mail address: luohx7@mail.sysu.edu.cn; yaodaox@mail.sysu.edu.cn;

This study describes the synthesis and characterization of Nb_2TiW and Nb_2TiMo medium-entropy alloys (MEAs). The Nb_2TiW and Nb_2TiMo MEAs can be successfully synthesized by an arc-melting method. Their structures and superconducting properties are investigated by detailed characterization of X-ray diffraction (XRD), resistivity, magnetization, and specific heat measurements. XRD results confirm that the obtained Nb_2TiW and Nb_2TiMo compounds have the same body-centered cubic (BCC) structures and crystalize in the $Im\bar{3}m$ space group (number 229). Experimental results show that the superconducting transition temperatures T_cs of Nb_2TiW and Nb_2TiMo are around 4.86 K and 3.22 K, respectively. The upper and lower critical fields of Nb_2TiW are 3.52(2) T and 53.36(2) Oe, respectively, and those of Nb_2TiMo are 2.11(2) T and 68.23(3) Oe, respectively. First-principles calculations reveal that the *d* electrons of Nb, Ti, and Mo or W are the dominant contribution of the density of states near the Fermi level. Specific heat measurement results indicate that Nb_2TiW and Nb_2TiMo display BCS full-gap *s*-wave superconductivity.

P*ACS*: 74.70.Dd, 74.62.Bf, 74.25.F-, 74.62.-c, 74.25.-q

Medium-entropy alloys (MEAs) and high-entropy alloys (HEAs) are a new class of metallic materials, the study of which has now developed into a cutting-edge direction involving the cross-fertilization of multiple disciplines such as materials, physics, chemistry, mechanics, and computational science.[1-9] Their unique atomic arrangement, crystal structure, and interaction mechanism have received significant attention in materials science, catalyst design, energy storage, and other fields.[10-12]

One of the most attractive properties of MEAs and HEAs in condensed matter physics is superconductivity. These solid solutions of MEAs and HEAs consist of multiple components and are characterized by a significant mixing entropy (ΔS_{mix}). One definition is based on the magnitude of the mixing entropy ΔS_{mix}, ΔS_{mix} is calculated by the following equation: $\Delta S_{mix} = -R\sum_{i=1}^{n} c_i \, ln \, c_i$, where n is the number of components, c_i is the atomic fraction, and R is the gas constant. According to this equation, the ΔS_{mix} of MEA is between 0.69 R~1.60 R. As the number of constituent elements in the solid solution increases, the ΔS_{mix} enhances accordingly. Depending on the magnitude of the desired ΔS_{mix}, low-entropy alloys are classified as those with R-values less than 0.69, whereas the R-values of HEAs are 1.60 or higher.[13] MEAs and HEAs are composed of three or more elements combined in the range of 5 - 35 % atomic.[14, 15] These MEAs and HEAs produce more compositional disorder (high ΔS_{mix}) than conventional alloys due to the difference in atomic size.[16] The $Ta_{34}Nb_{33}Hf_8Zr_{14}Ti_{11}$ HEA with a superconducting transition temperature of $T_c \approx 7.3$ K was the first high-entropy superconductor to be reported.[17] Since then, more and more MEA and HEA superconducting materials have been discovered.[18-21] To date, MEAs and HEAs superconductors possess many types of crystal structures, including body-centered cubic (BCC), face-centered cubic (FCC), hexagonal close-packed (HCP), CsCl-type, α-Mn-type[22-24] and so on. Recently, some MEAs superconducting materials have been developed and showed unique superconducting properties. The BCC-type TiHfNbTa MEA, for example, presents extremely coupled *s*-wave superconductivity [19]. In addition, TiZrHfNb MEA displays record-high T_c and dome-shaped superconductivity under applied pressure conditions [25]. Another HCP-type MoReRu MEA superconductor with a valence electron count (VEC = 7) has a T_c = 9.1 K [26].

Previous reports demonstrate that the VEC of MEA superconductors plays a crucial role in determining their T_cs, as well as the stability of the material [23, 27, 28]. On the other hand, the element Nb content also affects the superconducting temperature. Remarkably, the element Nb is the single element with the highest T_c at atmospheric pressure, with 9.23 K [19]. Therefore, the element Nb is commonly used in the design of superconducting materials for MEAs and HEAs. In addition, NbTi alloy is a well-known commercial superconducting material with excellent properties such as accessible T_c, high critical current density, high critical magnetic field, and easy processing [29-33]. Moreover, the T_c of NbTi alloys increases from ~ 9.6 K to ~ 19.1 K at high pressure. NbTi alloys are the most robust of the known stressed superconductors [34]. More recently, Nb_2TiW and Nb_2TiMo with the $Fm\bar{3}m$ structure was predicted to be superconducting and highly ductile, making them potential candidates for the fabrication of wires and strips for superconducting magnets [35]. By machine learning prediction, the Nb_2TiW compound shows the advantage of a large critical temperature, $T_c^{Eliashberg}$ = 11 K ($T_c^{McMillan}$ = 9 K) and energy above the convex hull (E_{hull}) = 25 meV/atom. Another compound, Nb_2TiMo is also at the lower of ductility hyperbole (G/B = 0.2

and (C_{12} - C_{44}) / E = 1.0), with the advantage of being more energy stable, only 25 meV/atom from the shell.

Based on the considerations mentioned above, we report the synthesis, crystal structure, and physical properties of Nb_2TiW and Nb_2TiMo compounds with VEC = 5 e/a. The ΔS_{mix} of the new MEA superconductors Nb_2TiW and Nb_2TiMo are ΔS_{mix} = 1.040 R, which lie between 0.69 and 1.60, and thus both are categorized as MEA. Our XRD results confirm that obtained Nb_2TiW and Nb_2TiMo MEA are adopted in the BCC structure, while it is different from the $Fm\bar{3}m$ structure used in prediction [35]. The T_cs of Nb_2TiW and Nb_2TiMo are 4.86 K and 3.22 K, respectively, as determined from electrical resistivity, magnetization, and specific heat measurements. Our specific heat measurements indicate that these two Nb_2TiW and Nb_2TiMo MEA are BCS full-gap *s*-wave superconductors.

The MEA Nb_2TiW and Nb_2TiMo compounds were synthesized by an extraordinary arc-melting method. The raw materials for the Nb_2TiW MEA were niobium from Macklin (99.99%, 325 mesh), titanium from Macklin (99.99%, 300 mesh), and tungsten from Macklin (99.5%, 325 mesh). Similarly, for the Nb_2TiMo MEA, we chose niobium from Macklin (99.99%, 325 mesh), titanium from Macklin (99.99%, 300 mesh), and molybdenum from Alfa Aesar (99.9%, 250 mesh). To begin the synthesis process, we carefully weighed a mixture of 250 mg of elemental powders in a precise 2:1:1 molar ratio. Then, a sample of all the powders was placed in a mortar and thoroughly ground for 1 hour to make a homogeneous mixture. We carefully pressed a pellet from this mixture. The pellet was transferred to an electric arc furnace and melted under a controlled argon environment at 0.5 atm. To ensure homogeneity throughout the material, we perform a series of turning and remelting procedures on the ingot to blend it to perfection. In the end, we obtained pure Nb_2TiW and Nb_2TiMo MEA materials.

The phase purity of the obtained compounds was characterized by powder X-ray diffraction (XRD). XRD data are collected with great precision, with an angular range of 10° to 100°, in steps as small as 0.01°. For the analysis, we use a Japanese Rigaku MiniFlex instrument equipped with Cu Kα radiation by continuously scanning at a constant rate of 1°/min. To refine and elucidate the XRD patterns, we used the Rietveld method, supplemented by the comprehensive FULLPROF software suite [36]. In addition, we used backscattered scanning electron microscopy (BSEM) and scanning electron microscope (SEM) to fully characterize the elemental proportions and microstructure of the Nb_2TiW and Nb_2TiMo materials (EVO, Zeiss). In addition, the EVO microscope has an integrated energy dispersive X-ray spectroscopy (EDXS) capability, which allowed us to analyze the elemental composition and distribution of the samples, thereby deepening our understanding of the sample microstructures. To gain insight into the superconducting behavior of the material, we carried out the resistivity using the physical property measurement system (PPMS, DynaCool-14T, Quantum Design). Our obtained samples were tested from 1.8 K to 300 K using a four-point probe technique. In addition to resistivity, we also reveal the magnetization properties through zero-field-cooling (ZFC) and field-cooling (FC) magnetization experiments. Finally, to understand the bulk nature of the superconducting properties of the samples, we also measured the specific heat of the material over the temperature range of 1.8 K to 15 K.

The density functional theory (DFT) calculations were performed using the Vienna ab initio simulation package (VASP) [37, 38]. The generalized gradient approximation (GGA) with the Perdew-Burke-Ernzerhof (PBE) exchange-correlation function was used in the DFT calculations [39]. The plane wave cutoff energy was set to be 600 eV, and a k-mesh grid of 9 × 9 × 9 centered at the Γ-point was sampled in the Brillouin zone. The total energy criterion at the self-consistent step and force convergences criteria were 10^{-6} eV and 0.001 eV/Å, respectively. The experimentally measured lattice constants of the MEAs were adopted in the DFT calculations. Spin-orbit coupling (SOC) was included in band structure calculations. To describe the chemical disorder in the MEAs, the 2 × 2 × 2 supercells special quasi-random structures (SQSs) with 16 atoms were utilized, which are modeled by Monte Carlo Special Quasi-random Structure as implemented in the Alloy Theoretic Automated Toolkit [40, 41].

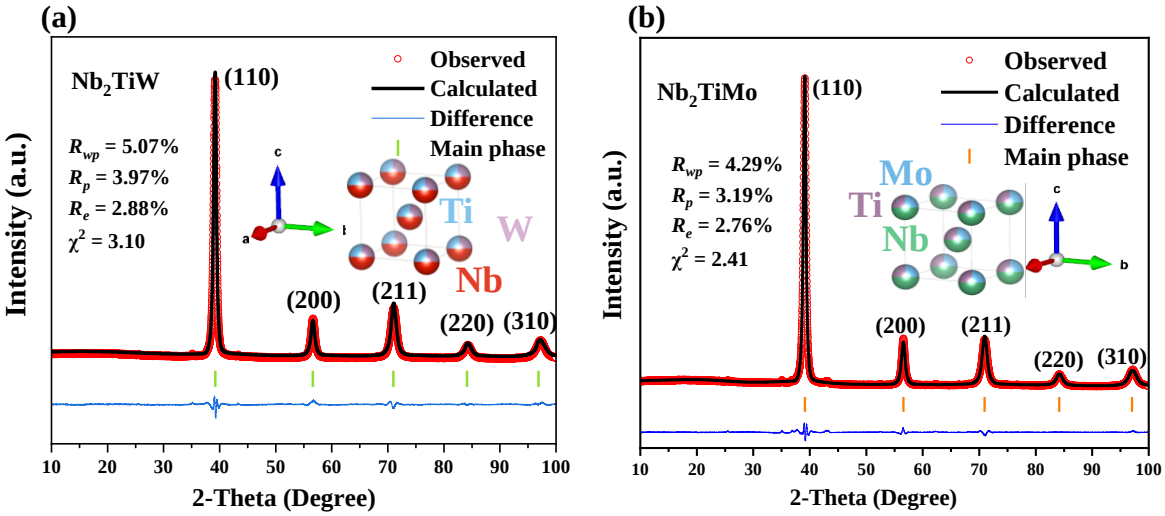

Fig. 1. (a) XRD refinement of Nb_2TiW. The inset shows the crystal structure of Nb_2TiW MEA alloy with $Im\bar{3}m$ space (b) XRD refinement of Nb_2TiMo. The inset shows the crystal structure of Nb_2TiMo MEA alloy with $Im\bar{3}m$ space.

The X-ray diffraction (XRD) spectra of the MEA Nb_2TiW and Nb_2TiMo superconducting samples and the results of their correlation analyses are presented in Fig. 1(a) and Fig. 1(b), respectively. Based on the XRD spectra, the products can be identified as pure Nb_2TiW and Nb_2TiMo superconducting materials. For ease of labeling, all observed XRD peaks were labeled with their respective Miller indices. In addition, the mild expansion of the peak signals is due to the highly disordered structure. It was relatively easy to index the XRD data in the BCC structure, where the space group $Im\bar{3}m$ and the identification number No. 229 were used. It is different from the previous prediction using pace group $Fm\bar{3}m$ (No. 225). Fitting the XRD profiles by Rietveld refinement, the values of the refinement parameters R_{wp}, R_p, R_e, and χ^2 for the MEA Nb_2TiW samples were 5.07 %, 3.97 %, 2.88 %, and 3.10, respectively. The values of refinement parameters R_{wp}, R_p, R_e, and χ^2 for the MEA Nb_2TiMo samples were 4.29 %, 3.19 %, 2.76 % and 2.41, respectively. These fitting data indicate that the fit is good. The final lattice parameters of the MEA Nb_2TiW and Nb_2TiMo crystals were obtained as $a = b = c = 3.248(11)$ Å and $a = b = c = 3.247(17)$ Å. The crystal structures of the Nb_2TiW and Nb_2TiMo superconducting samples are shown in the

insets of Fig. 1(a) and Fig. 1(b), respectively. It can be seen that both compounds have BCC crystal structures, and the three elemental atoms Nb, Ti, and W in Nb_2TiW randomly occupy the lattice sites. In addition, the homogeneity and chemical composition of the Nb_2TiW and Nb_2TiMo samples were characterized using SEM-EDXS. Fig. S1(a) and Fig. S1(b) present the ratios of the constituent elements, which, according to the accurate chemical formulae, are $Nb_{2.3}Ti_{0.8}W_{0.9}$ and $Nb_{1.9}Ti_{1.2}Mo_{0.9}$. The actual elemental ratios are very close to the design values, suggesting that the prepared samples are as expected. The minor deviations may be caused by the limited precision of EDXS and the unevenness of the sample surface. From the SEM and BSEM images in Fig. 2, as well as the elemental mapping using EDX, we can observe that the studied Nb_2TiW and Nb_2TiMo compounds are homogeneous under the microscope. These results reveal the crystal structure, chemical composition, and homogeneity characteristics of the Nb_2TiW MEA and Nb_2TiMo MEA superconducting samples, which provide the basis and foundation for confirming the purity and the actual elemental content of the MEA Nb_2TiW and Nb_2TiMo superconducting samples.

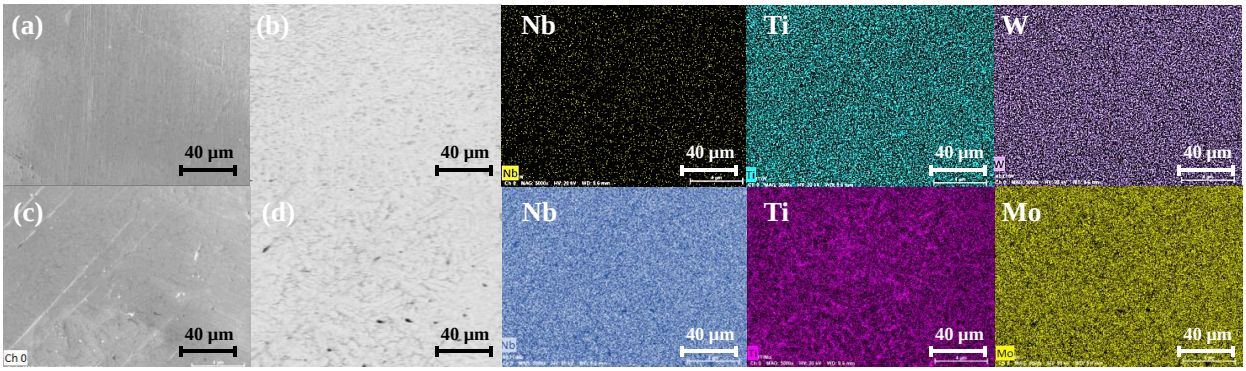

Fig. 2. (a) SEM image mapping of the Nb_2TiW MEA, (b) BSEM spectrum mapping of the Nb_2TiW MEA, and EDX elemental mappings of the Nb_2TiW MEA. (c) SEM image mapping of the Nb_2TiMo MEA. (d) BSEM spectrum mapping of the Nb_2TiMo MEA and EDX elemental mappings of the Nb_2TiMo MEA.

Resistivity testing is a commonly used experimental method to evaluate the performance characteristics of superconducting materials. In this study, we show the variation of normalized resistivity ($\rho/\rho_{300\ K}$) in the temperature range of 1.8 ~ 300 K for Nb_2TiW and Nb_2TiMo MEA samples in Fig. 3(a) and Fig. 3(c), respectively. For the Nb_2TiW MEA sample, the resistivity exhibits metallic behavior as the temperature decreases from 300 K to about 6 K. The resistivity of the samples is also shown in the normalized resistivity ($\rho/\rho_{300\ K}$) for the Nb_2TiW MEA sample. For the Nb_2TiMo MEA sample, the resistivity similarly exhibits metallic behavior as the temperature decreases from 300 K to about 4 K. The resistivity of the Nb_2TiMo MEA sample shows a metallic behavior at lower temperatures. However, at much lower temperatures, the resistivity drops dramatically and tends to zero, clearly showing the presence of superconducting properties. The Residual Resistivity Ratio (*RRR*) is a key parameter in our research as it is an indicator of the electronic properties and quality of the material under study [42-44]. In general, higher *RRR* values indicate lower levels of impurities and defects, which are essential to ensure structural homogeneity and excellent electrical conductivity in metallic systems [43]. Here, our calculated *RRR* value is the ratio of the resistivity of the samples at 300 K and 5 K, which is used

to evaluate the purity and conductivity of the samples. We calculated the RRR = R_{300K}/R_{5K}. For the Nb_2TiW superconductor, we measured its resistivity values to be 32.91 μΩ-cm at 300 K and 21.78 μΩ-cm at 5 K. The resulting *RRR* value for Nb_2TiW is therefore R_{300K}/R_{5K} = 1.51. Similarly, for Nb_2TiMo the resistivity value is 144.92 μΩ-cm at 300 K and 99.38 μΩ-cm at 5 K. Therefore, the *RRR* value for Nb_2TiMo is R_{300K}/R_{5K} = 1.46. Both of them are relatively low values, comparable to that observed for nonstoichiometric or highly disordered intermetallic compounds [23, 27, 28].

To describe the superconducting behavior of the two materials more specifically, Fig.3(b) and Fig. 3(d) demonstrate the resistivity trend over the temperature range of 1.8 ~ 10 K and 1.8 ~ 5 K, respectively. The resistivity of the two materials is shown in Fig. 3(a) and Fig. 3(c). We determined the T_c using a 50 % reduction in resistivity relative to the value at the normal state. By analyzing the data, we determined the T_c of the Nb_2TiW and Nb_2TiMo MEA superconductors to be about 4.86 K and 3.22 K, respectively. It is noteworthy that the resistivity of the Nb_2TiW MEA superconductor reaches zero at about 4.45 K. Also, at about 3.13 K, the resistivity of the Nb_2TiMo MEA superconductor reaches zero. These indicate the presence of its superconducting nature. It is worth noting that the range over which the resistivity undergoes drastic changes is very narrow. These results are crucial for our in-depth understanding and evaluation of the superconducting properties and performance characteristics of the Nb_2TiW and Nb_2TiMo MEA superconductors and provide a valuable reference for future applications and research of superconducting materials.

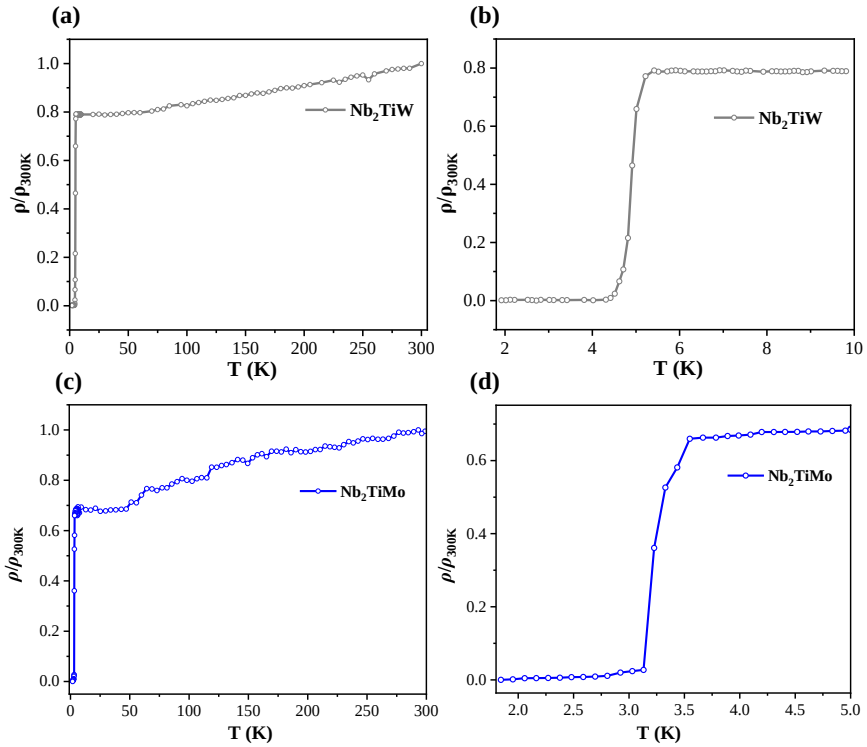

Fig. 3. (a) Temperature dependence of normalized ρ/ρ_{300K} of the Nb_2TiW sample. (b) Low-temperature behavior of Nb_2TiW MEA near T_c. (c) Temperature dependence of normalized ρ/ρ_{300K} of the Nb_2TiMo sample. (d) Low-temperature behavior of Nb_2TiMo MEA near T_c.

Fig. 4(a) and Fig. 4(b) show the magnetization versus temperature of the Nb_2TiW MEA and Nb_2TiMo MEA superconductor under an applied magnetic field of 30 Oe in the temperature range of 1.8 - 8 K and 1.8 - 6 K, respectively. The measurements were performed under ZFC and FC. The diameters and heights of the two cylindrical samples Nb_2TiW and Nb_2TiMo are 3 mm×4 mm and 2.5 mm×3 mm, respectively. The demagnetization factors are corrected according to the shape of the cylindrical samples by using the corresponding demagnetization factor formula, $N^{-1} = 1+ 1.6\frac{c}{a}$. The demagnetization factors of Nb_2TiW and Nb_2TiMo are about 0.3[45]. The trend of rapid decrease of magnetization with temperature in Nb_2TiW MEA and Nb_2TiMo MEA superconductors is confirmed by the strong diamagnetic signals observed at T_c = 4.66 K and T_c = 3.21 K, which confirm the presence of superconductivity in Nb_2TiW and Nb_2TiMo, respectively. To obtain a more accurate magnetization profile, the isothermal magnetization M(H) data were measured at 1.8 K. Fig. 4(c) and Fig. 4(d) shows the magnetic isotherm measured in the temperature range of 1.8 - 3.6 K for Nb_2TiW and 1.8 - 2.6 K for Nb_2TiMo. Under the assumption of a perfect magnetic field response, the equation for the linear fit in the low magnetic field region is $M_{fit} = m+ nH$, where m is the intercept and n is the slope of the straight line [46]. Fig. S2 illustrates the M-M_{fit} curves at

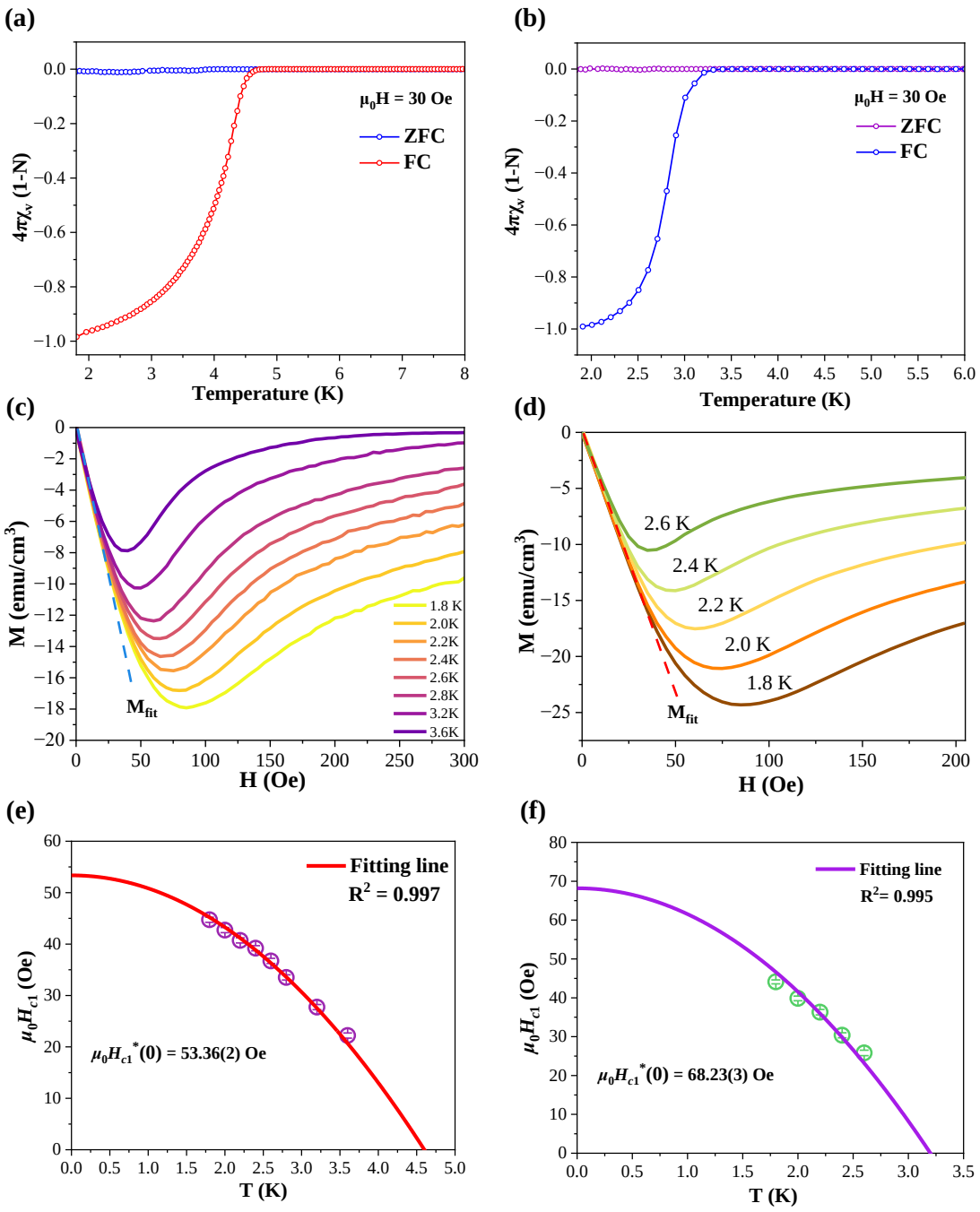

Fig. 4. (a) and (b) Magnetic susceptibilities for Nb_2TiW and Nb_2TiMo at the superconducting transitions, applied DC fields are 30 Oe. (c) and (d) The isothermal magnetization curve of the Nb_2TiW within the range of 1.8 to 3.6 K and Nb_2TiMo superconductor within the range of 1.8 to 2.6 K. (e) and (f) The temperature dependence of the effective lower critical field of the Nb_2TiW and Nb_2TiMo superconductor, respectively.

different temperatures. Usually, the value of $\mu_0 H_{c1}(0)$ is extracted when the difference between M and M_{fit} exceeds 1% M_{max}. The obtained points shown in the main panels of Fig.4(c) and Fig. 4(d)

fit well into the empirical formula: $\mu_0 H^*_{c1}(T) = \mu_0 H^*_{c1}(0)(1-(T/T_c)^2)$, where T_c is the superconducting transition temperature and $\mu_0 H_{c1}(0)$ is the lower critical field at 0 K. Thus, the lower critical magnetic field $\mu_0 H_{c1}(0)$ = 53.36(2) Oe for Nb_2TiW and $\mu_0 H_{c1}(0)$ = 68.23(3) Oe for Nb_2TiMo can be calculated exactly.

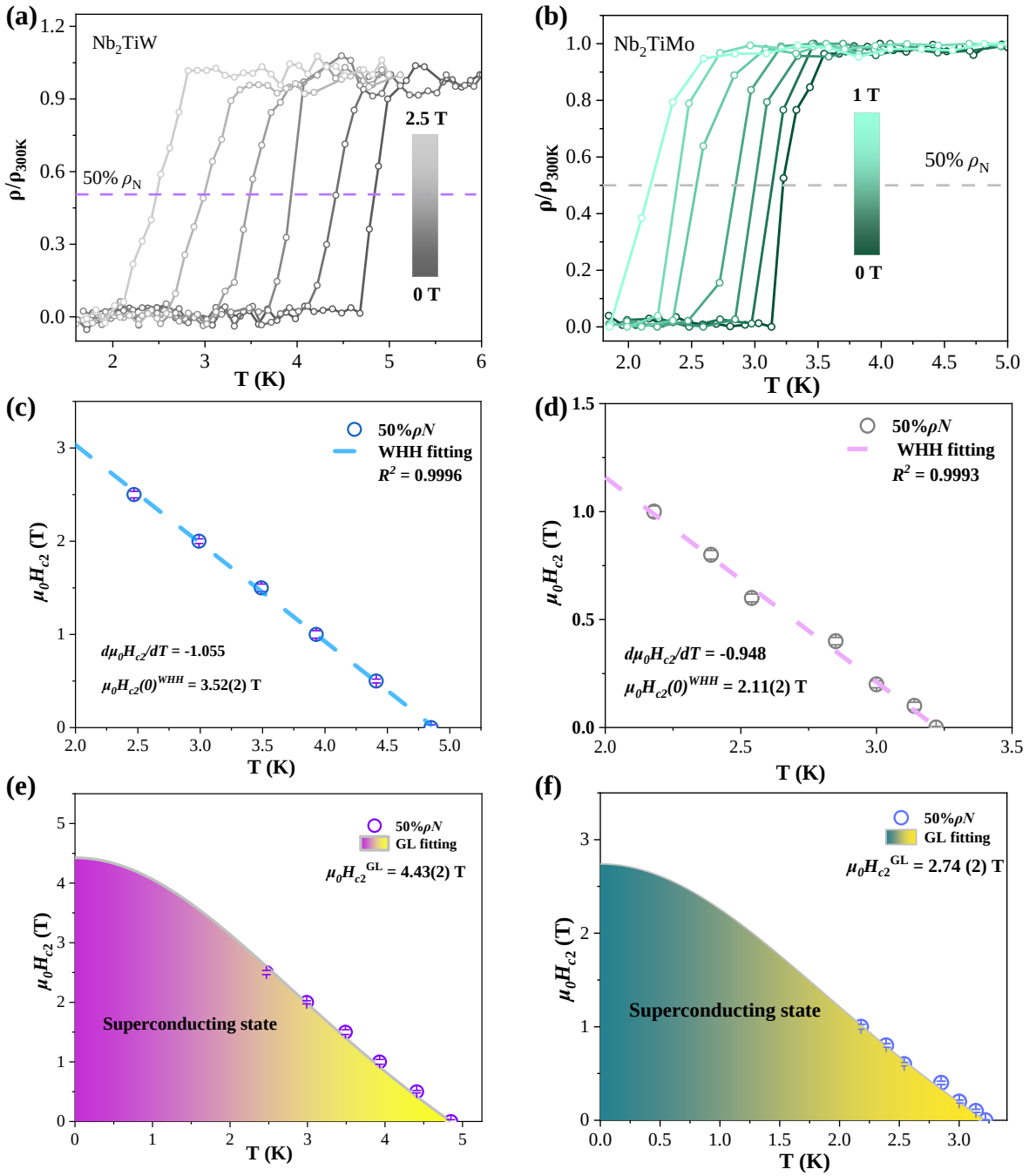

Fig. 5. (a) The resistivity of Nb_2TiW MEA under superconducting temperatures with the applied magnetic fields from 0 to 2.5 T. (b) The resistivity of Nb_2TiMo MEA under superconducting temperatures with the applied magnetic fields from 0 to 1.0 T. (c) The temperature dependence of the $\mu_0 H_{c2}$ and the WHH model fitting of Nb_2TiW MEA. (d) The temperature dependence of the

$\mu_0 H_{c2}$ and the WHH model fitting of Nb_2TiMo MEA. (e) The $\mu_0 H_{c2}$-T phase diagram of the Nb_2TiW MEA superconductor. (f) The $\mu_0 H_{c2}$-T phase diagram of Nb_2TiMo MEA superconductor.

In addition, to gain a deeper understanding of the superconducting properties of Nb_2TiW and Nb_2TiMo MEA, the resistivity data of Nb_2TiW and Nb_2TiMo MEA superconductors were investigated using the R-T measurement system at various fixed magnetic fields. Fig. 5(a) demonstrates the low-temperature resistivity of Nb_2TiW MEA at different magnetic fields in the magnetic field range 0 - 2.5 T. Meanwhile, Fig. 5(b) depicts the low-temperature resistivity of Nb_2TiMo MEA under the magnetic field magnetic field range of 0 - 1.0 T. At low temperatures, SC exhibits a sharp decrease in ρ(T) down to the value of $\rho = 0$. When T_c is defined as a 50% decrease in resistivity related to the normal state value, the transition temperatures of the ρ(T) data for Nb_2TiW and Nb_2TiMo MEA superconductors are categorized as $T_c = 4.86$ K and $T_c = 3.22$ K. When the magnetic field is increased, the T_c shifts to lower temperatures and the superconducting transition becomes wider. We obtained the temperature variation of $\mu_0 H_{c2}(0)$ for Nb_2TiW and Nb_2TiMo MEA samples. The slope ($d\mu_0 H_{c2}/dT$) of the Nb_2TiW MEA compound is -1.055 T/K, as shown in Fig. 5(c). The slope ($d\mu_0 H_{c2}/dT$) of the Nb_2TiMo MEA compound is -0.948 T/K, as shown in Fig. 5(d). The data were fitted with the WHH formula: $\mu_0 H_{c2}(0) = -0.693 T_c (\frac{d\mu_0 H_{c2}}{dT})|_{T=Tc}$. Using $T_c = 4.86$ K (50% ρN), the dirty limit $\mu_0 H_{c2}(0)$ WHH value for the Nb_2TiW MEA superconductor was calculated to be 3.52(2) T. Using the same fit with the WHH formula, using $T_c = 3.22$ K (50% ρN), the dirty limit $\mu_0 H_{c2}(0)$ WHH value for the Nb_2TiMo MEA superconductor was calculated to be 2.11(2) T. In order to explore the properties of Nb_2TiW and Nb_2TiMo MEA more precisely, we defined the resistivity value as low as 50% of ρ_N as $\mu_0 H_{c2}$ and calculated $\mu_0 H_{c2}(0)$ using the Ginzburg-Landau (GL) equation: $\mu_0 H_{c2}(T) = \mu_0 H_{c2}(0) \times \frac{(1-(T/T_c)^2}{(1+(T/T_c)^2}$. Fitting the data yields $\mu_0 H_{c2}(0)^{GL} = 4.43(2)$ T for Nb_2TiW and $\mu_0 H_{c2}(0)^{GL} = 2.74(2)$ T for Nb_2TiMo MEA. Thus, the phase diagrams of $\mu_0 H_{c2}(0)$ relative to T for Nb_2TiW and Nb_2TiMo MEA are shown in Fig. 5(e) and Fig. 5(f). The GL model satisfactorily fits the experimental data over the entire temperature range. It is worth noting that the upper critical field calculated by the WHH model and the GL model must be smaller than the Pauli limit field. The $\mu_0 H^{\text{Pauli}} = 1.86 T_c = 9.04$ T for Nb_2TiW an $\mu_0 H^{\text{Pauli}} = 1.86 T_c = 5.99$ T for Nb_2TiMo derived from the Pauli limit effect are both larger than the upper critical field [47].

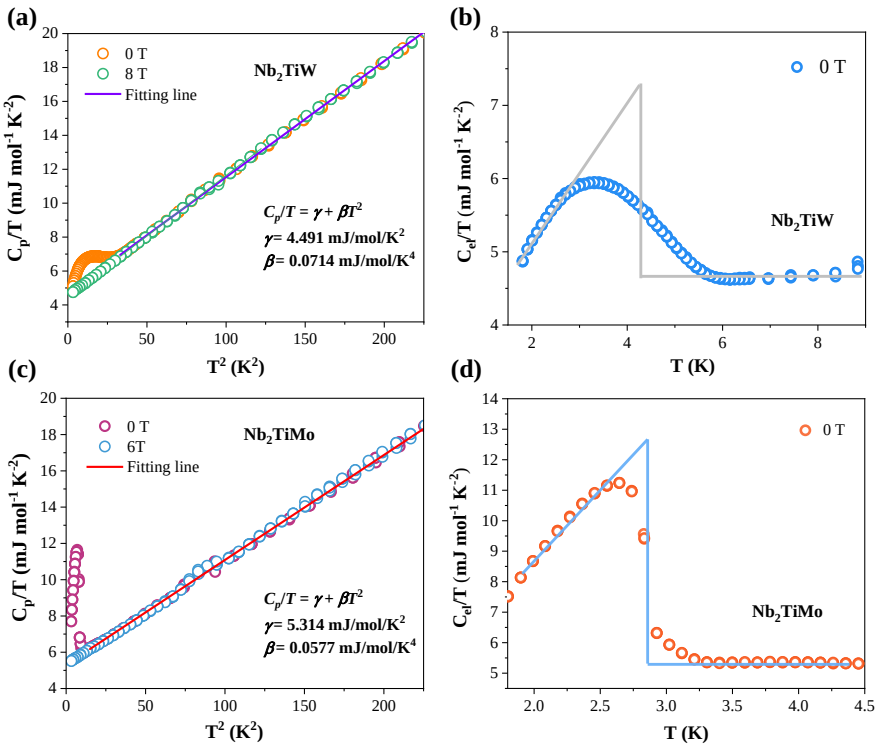

Fig. 6. Specific heat curves of Nb_2TiW MEA and Nb_2TiMo MEA at zero magnetic field. (a) Nb_2TiW MEA specific heat coefficient C_p/T as a function of T^2. (b) Nb_2TiW MEA electron contribution to heat capacity as a function of C_{el}/T. (c) Nb_2TiMo MEA specific heat coefficient C_p/T as a function of T^2. (d) Nb_2TiMo MEA electron contribution to heat capacity as a function of C_{el}/T.

The bulk superconducting states of Nb_2TiW MEA and Nb_2TiMo MEA are further supported by heat capacity measurements, as shown in Fig. 6. In the normal state above T_c, the data points can be fitted by the equation $C_p/T = \gamma_n + \beta T^2$, where γ_n denotes the Sommerfeld constant for the normal state, and β denotes the specific heat coefficient of the lattice part. The fitted data obtained from this equation for Nb_2TiW and Nb_2TiMo are shown in Fig. 6(a) and Fig. 6(c) for γ_n(W) = 4.681 mJ/mol/K^2 and β(W) = 0.0685 mJ/mol/K^4 and γ_n(Mo) = 5.314 mJ/mol/K^2 and β(Mo) = 0.0577 mJ/mol/K^4, respectively. Fig. 6(b) and Fig. 6(d) show the C_{el}/T - T curves for the temperature ranges of 1.8 K to 10 K and 1.8 K to 4.5 K, respectively, where the C_{el} is obtained from the equation $C_{el} = C_p - \beta T^3$. Estimates determined from the equal-area entropy structure are consistent with T_c extracted from resistivity and magnetization measurements. The Nb_2TiMo normalized specific heat jump value $\Delta C_{el}/\gamma_n T$ = 1.35(3), slightly below the Bardeen-Cooper-Schrieffer (BCS) weak coupling limit value of 1.43 for bulk SC. The Nb_2TiW normalized specific heat jump value $\Delta C_{el}/\gamma_n T$ = 0.81(2). The Debye temperature (Θ_D) was then estimated using the Debye model, and the value in the equation $\Theta_D=(12\pi^4 nR/5\beta)^{1/3}$, where R denotes the gas constant and n denotes the number of atoms in the formula cell. The estimated Θ_D values for Nb_2TiW and Nb_2TiMo are 304 K and 322 K, respectively. Given the Θ_D and T_c, the semi-empirical McMillan

formula was used: $\lambda_{ep}=\frac{1.04+\mu^{*}\ln\left(\frac{\Theta_D}{1.45T_c}\right)}{\left(1-1.62\mu^{*}\right)\ln\left(\frac{\Theta_D}{1.45T_c}\right)-1.04}$.[48] The calculation of the electron-phonon coupling constants λ_{ep} = 0.63 for Nb_2TiW and λ_{ep} = 0.55 for Nb_2TiMo with μ^* = 0.13 are obtained. In addition, it is also possible to estimate the value of DOS located in the Fermi energy level $N(E_F)$ by using the formula $N(E_F)=\frac{3}{\pi^2 k_B^2(1+\lambda_{ep})}\gamma$ with the values of γ and λ_{ep}. The obtained $N(E_F)$ for the Nb_2TiW and Nb_2TiMo samples are 1.22 states eV^{-1} $f.u.^{-1}$ and 1.46 states eV^{-1} $f.u.^{-1}$, respectively.

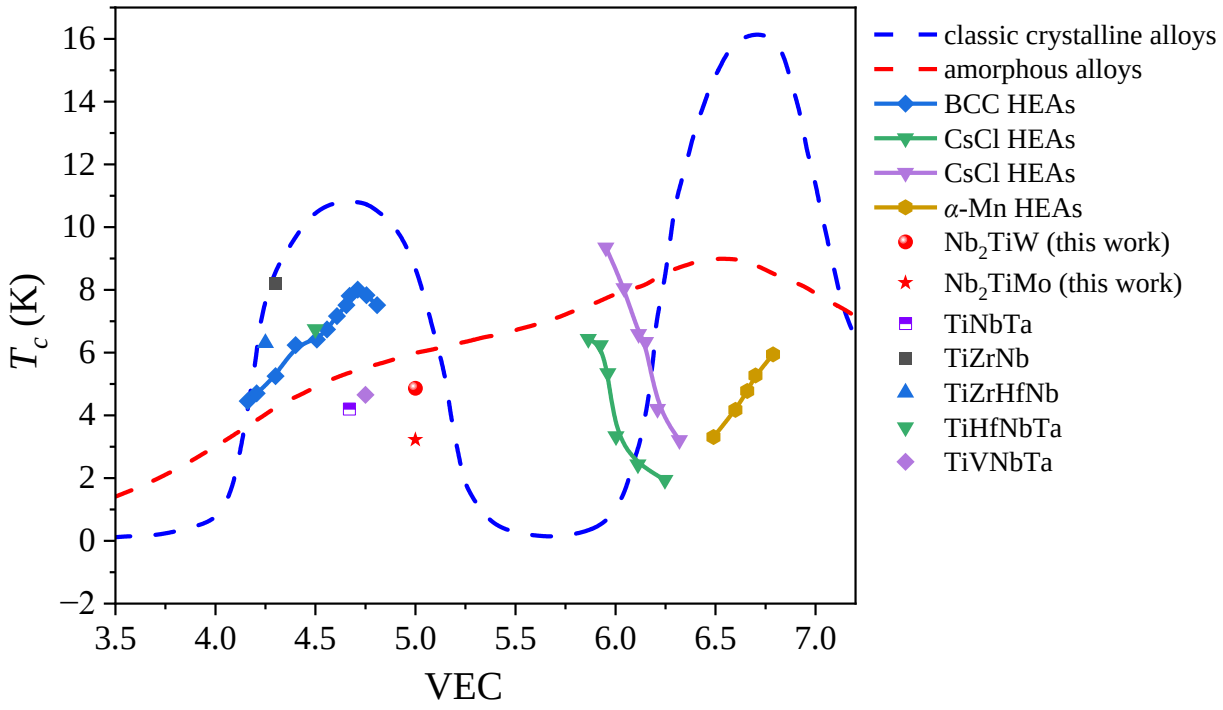

Fig. 7. The phase diagram of VEC-T_c for BCC HEAs, CsCl HEAs, amorphous alloys, classic crystalline alloys, Nb_2TiW and Nb_2TiMo systems.

The phase stability of crystalline solid solutions with slight differences in atomic size is critically influenced by a parameter VEC [5]. For MEA and HEA, calculating the number of valence electrons per alloy is a critical step in designing synthetic superconducting materials. We compare the T_cs and VEC of crystalline transition metals and their alloys, amorphous vapor deposition films, BCC-type HEAs, CsCl-type HEAs and α-Mn-type HEAs superconductors to summarize the relationship between them in Fig. 7[17, 18, 20, 23, 27, 28, 49-52]. Nb_2TiW and Nb_2TiMo are marked with a red dot and a red five-pointed star in the diagram, respectively. The T_c with VEC for Nb_2TiW and Nb_2TiMo is comparable to other reported bcc-type MEA and HEA superconductors. Notably, the VEC of MEA superconductors plays a crucial role in determining their T_c and material stability. The T_c of MEA superconductors is strongly dependent on the VEC, as seen in the Matthias plots of T_c versus electron counts in simple binary transition metal alloys. Comparing the superconducting transition temperatures of crystalline transition metals and their alloys [53],

amorphous deposited thin films [54] and BCC-type HEA superconductors, it is found that the T_cs of HEA superconductors is significantly lower than that of the crystalline alloys, and the value shows a monotonically increasing trend higher than that of the amorphous alloys. This suggests that crystallinity has a significant effect on T_c when comparing crystalline binary alloys, HEAs, and amorphous materials at the same electron counts. It is worth noting that a detailed physical comparison between amorphous superconductors, HEA superconductors, and binary superconductors has not yet been performed, but it suggests that the ambiguity of the electron energy (*E*) versus the electron wavevector (*k*) leading to disorder-induced increases in the density of electronic states may be responsible for this behavior. Considering all these results, it can be inferred that a more desirable crystallinity has a positive effect on the T_c of alloys. When considering the T_c of all three superconductors, a trend in all-electron counting can be observed. The small-crystallite BCC-type and CsCl-type HEA superconductors seem to generally follow the bimodal character of the simpler binary alloys with VECs around 4.7 and 5.9, whereas the more complex α-Mn-type HEA superconductors do not seem to follow the general trend of the other two systems. Temperature changes induced by atomic substitutions, particularly through the VEC, appear to be a general behavior in HEA superconductors. The T_c of BCC-type superconductors increases with increasing VEC, reaching a maximum value of 7.3 K near 4.7. Similarly, a relationship between the VEC and the T_c has been observed for CsCl-type superconductors, with superconductivity occurring at VECs in the range of 5.9 - 6.3, with a maximum T_c of 9.3 K occurring at a VEC of about 5.9. Therefore, we believe that considering the relationship between VEC and T_c in the exploration of predicting, designing, and synthesizing MEA and HEA superconductors is an effective way to discover new superconducting materials.

To gain more insight into the physical properties of Nb_2TiMo and Nb_2TiW, we performed DFT calculations to study their electronic structures. Fig. 8 displays the calculated total density of states (DOS) and projected DOS of Nb_2TiMo (left panel) and Nb_2TiW (right panel). Considering the chemical disorder in the alloys, we employed three different SQSs for each formula, and the average DOS of three SQSs is given in Fig. 8. As shown in the top panel of Fig. 8, the total DOSs of both systems cross the Fermi level, suggesting their metallic properties. The DOSs at the Fermi level are about 2.84 states/eV/f.u. for Nb_2TiMo and 2.76 states/eV/f.u. for Nb_2TiW. With the calculated DOSs at the Fermi level, the theoretical Sommerfeld constants are estimated to be $\gamma_{Mo} = 6.69\, mJ \cdot mol^{-1} \cdot K^{-2}$ and $\gamma_W = 6.51\ mJ \cdot mol^{-1} \cdot K^{-2}$ through the relationship $\gamma = \frac{1}{3}\pi^2 k_B^2 N_A N(E_F)$, which is close to the experimental values. The local DOS diagrams indicate that Nb and Ti atoms contribute the most to the TDOS near the Fermi level, while Mo or W has a smaller contribution. Furthermore, *d* orbital plays a dominant role near the Fermi level, namely 3*d* for Ti, 5*d* for W, and 4*d* for Nb and Mo, while *p* orbital has less contribution, as the projected DOSs reveal. These results imply that the superconductivity may originate from the *d* electrons of Nb, Ti, and Mo or W, which could introduce strong couplings into the systems.

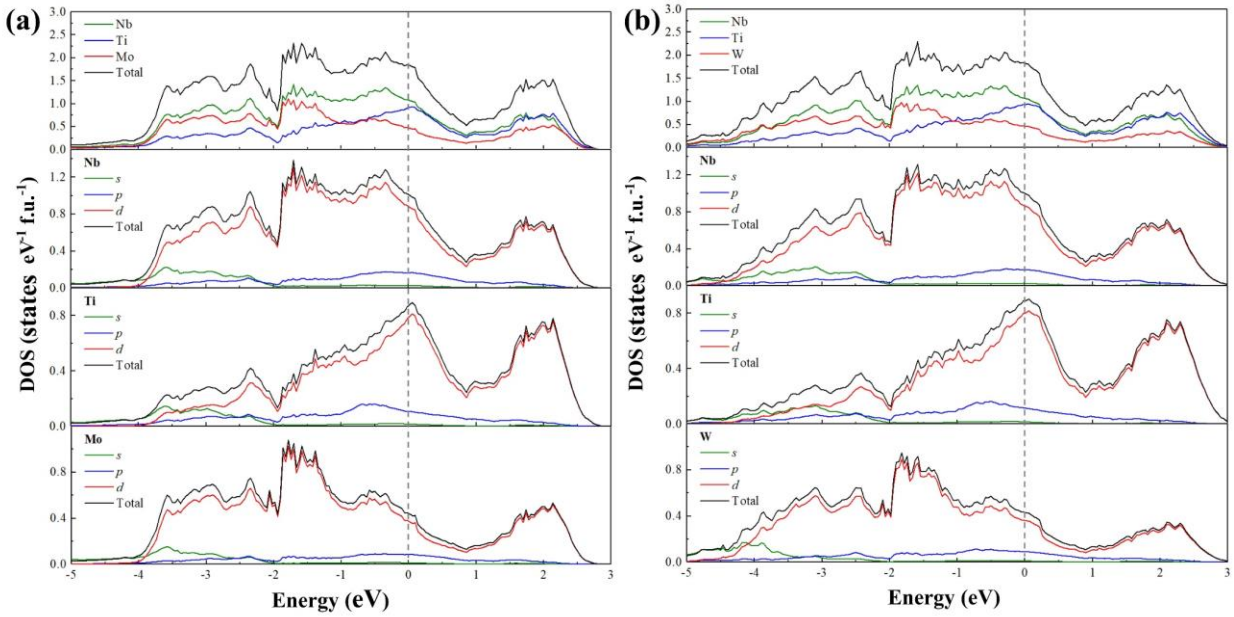

Fig. 8. Local DOS of each element and projected DOS with angular momentum decomposition of each element of Nb_2TiMo (a) and Nb_2TiW (b). The average DOSs of three structures built by mcsqs (as shown in Fig. S3) are adopted. The gray dashed lines indicate the Fermi level.

In recent years, several HEAs have been reported to host nontrivial band topology [21, 55]. Furthermore, chemical disorder in these HEAs can have influence on the position of Dirac points. Since MEAs share many characterics with HEAs, especially chemical disorder, it is of significance to investigate the topological aspect as well as disorder effect of Nb_2TiMo and Nb_2TiW. Therefore, we calculated the band structures of three representative special quasi-random structures (as shown in Fig. S3 in Supporting Information). As Fig. 9 displays, band structures of Nb_2TiMo [Fig. 9 (a-c)] and Nb_2TiW [Fig. 9 (d-f)] show similar features around the Fermi level, indicating that disorder has a modest effect on the electronic properties. Nb and Ti atoms have the largest contributions near the Fermi level, showing consistency with local DOS in Fig. 8. All six structures have dense and complex bands in the vicinity of the Fermi level, resulting in considerable DOSs at the Fermi energy. Note that there are several band-crossing features near the Fermi level, especially around the Z and Γ points, which imply possible topological states. However, as we further analyze, either they split due to the SOC effect originating from *d* electrons or no band inversion exists around the crossing. Thus, we suppose they are not Dirac points.

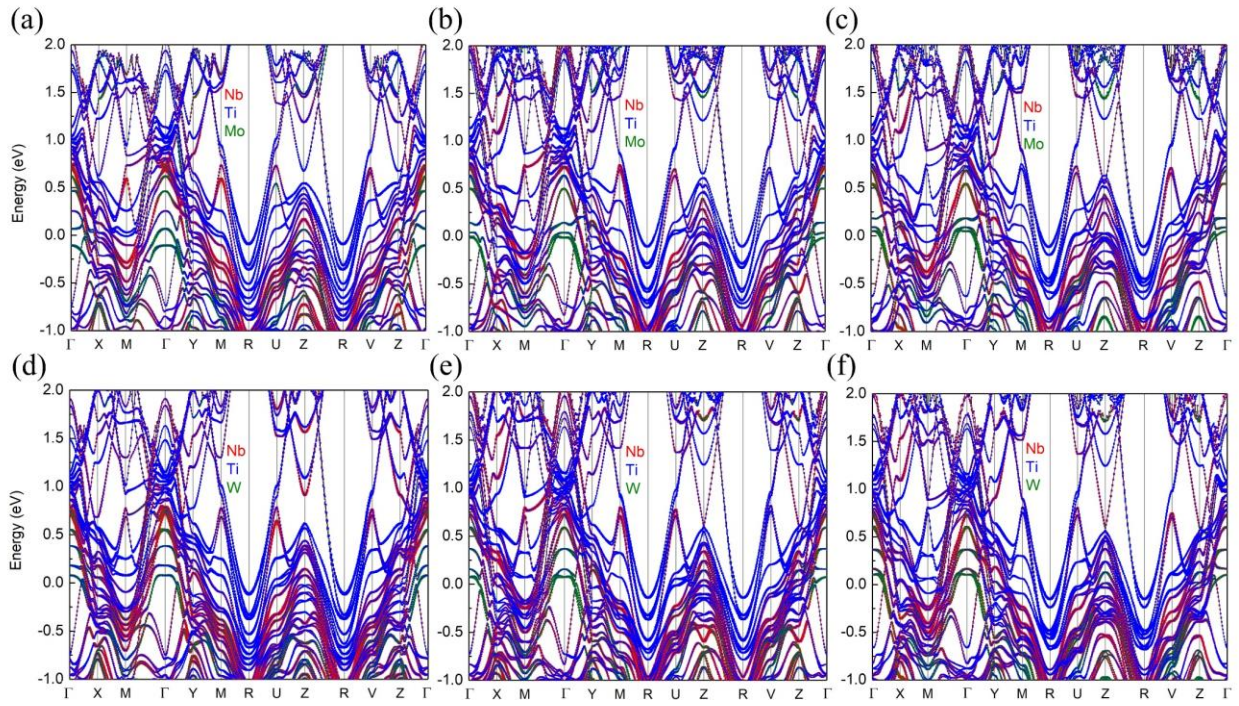

Fig. 9. Band structures of three representative SQSs of Nb_2TiMo (a-c) and Nb_2TiW (e-f) when SOC is considered in DFT calculations. The first, second and third columns are band structures of representative SQSs in Fig. S3 (a)-(c). The red, blue, and olive colors indicate the projection of Nb, Ti, Mo (a-c), and W (e-f). The Fermi level is set to zero.

We have successfully synthesized the new superconductors Nb_2TiW and Nb_2TiMo MEAs by arc-melting method. XRD results indicated that these two compounds crystallized in BCC structure (Space Group $Im\bar{3}m$, No. 229). The crystal structures of our experimental obtained Nb_2TiW and Nb_2TiMo compounds differ from the previous theory structures. Resistivity, magnetic and specific heat measurements suggest that Nb_2TiW has a T_c of 4.86 K, $\mu_0H_{c1}(0)$ ~ 53.36(2) Oe, and $\mu_0H_{c2}(0)$ ~ 3.52(2) T. Meanwhile, Nb_2TiMo has a T_c of 3.22 K, $\mu_0H_{c1}(0)$ ~ 68.23(3) Oe, and $\mu_0H_{c2}(0)$ ~ 2.11(2) T. Nb_2TiW and Nb_2TiMo MEAs are BCS full-gap *s*-wave superconductors verified by the specific heat measurements. In addition, we studied the band structures of different structural configurations. Similar features were observed near the Fermi level, indicating that the disorder has a moderate effect on the electronic properties. Nb and Ti atoms contribute the most near the Fermi level. By machine learning prediction, Nb_2TiW is an ordered structure, crystalizing in $Fm\bar{3}m$ space group. However, both Nb_2TiW and Nb_2TiMo in our study are MEAs, resulting in the disordered structures. The disorder in MEAs can renormalize electron-phonon/electron-electron interactions and change the phase coherence of Cooper pairs, and thus suppress superconductivity. Therefore, we suppose the discrepancy of T_c could be attributed to structural disorder. It is noteworthy that these materials are expected to be ductile, making them promising for practical applications in generating strong magnetic fields.

Notes

The authors declare no competing financial interest.

Reference

[1] Yeh J W, Chen S K, Lin S J, Gan J Y, Chin T S, Shun T T, Tsau C H and Chang S Y 2004 *Adv. Eng. Mater.* **6** 299
[2] George E, Raabe D and Ritchie R 2019 *Mater.* **4** 515
[3] Ye Y, Wang Q, Lu J, Liu C and Yang Y 2016 *Mater. Today* **19** 349
[4] Miracle D B and Senkov O N 2017 *Acta Mater.* **122** 448
[5] Sun L and Cava R J 2019 *Phys. Rev. Mater.* **3** 090301
[6] Cantor B, Chang I, Knight P and Vincent A 2004 *Mater. Sci. Eng.: A* **375** 213
[7] Gorsse S, Nguyen M, Senkov O N and Miracle D B 2018 *Data in brief* **21** 2664
[8] Senkov O, Wilks G, Miracle D, Chuang C and Liaw P 2010 *Intermetallics* **18** 1758
[9] Soni V, Senkov O, Gwalani B, Miracle D and Banerjee R 2018 *Sci. rep.* **8** 8816
[10] Saidi W A, Shadid W and Veser G t 2021 *J. Phys. Chem. Lett.* **12** 5185
[11] Zhou Y, Shen X, Qian T, Yan C and Lu J 2023 *Nano Res.* **16** 7874
[12] Ma J and Huang C 2023 *J. Energy Storage* **66** 107419
[13] Otto F, Yang Y, Bei H and George E P 2013 *Acta Mater.* **61** 2628
[14] Yeh J W, Chen S K, Lin S J, Gan J Y, Chin T S, Shun T T, Tsau C H and Chang S Y 2004 *Adv. Eng. Mater.* **6** 299
[15] Kitagawa J, Hamamoto S and Ishizu N 2020 *Metals* **10** 1078
[16] He B, Zu Y and Mei Y 2023 *J. Alloys Compd.* **958** 170479
[17] Koželj P, Vrtnik S, Jelen A, Jazbec S, Jagličić Z, Maiti S, Feuerbacher M, Steurer W and Dolinšek J 2014 *Phys. Rev. Lett.* **113** 107001
[18] Li K, Hu X, Guo R, Jiang W, Zeng L, Li L, Yu P, Wang K, Zhang C and Guo S 2023 *The J. Phys. Chem.* **127** 16211
[19] Zeng L, Hu X, Boubeche M, Li K, Li L, Yu P, Wang K, Zhang C, Jin K and Yao D-X 2023 *Science China Physics, Mech. Astron.* **66** 277412
[20] Zeng L, Zhan J, Boubeche M, Li K, Li L, Yu P, Wang K, Zhang C, Jin K and Sun Y 2023 *Adv. Quantum Technol.* **6** 2300213
[21] Zeng L, Wang Z, Song J, Lin G, Guo R, Luo S C, Guo S, Li K, Yu P and Zhang C 2023 *Adv. Funct. Mater.* **33** 2301929
[22] Marik S, Motla K, Varghese M, Sajilesh K, Singh D, Breard Y, Boullay P and Singh R 2019 *Phys. Rev. Mater.* **3** 060602
[23] Stolze K, Tao J, von Rohr F O, Kong T and Cava R J 2018 *Chem. Mater.* **30** 906
[24] Stolze K, Cevallos F A, Kong T and Cava R J 2018 *J. Mater. Chem. C* **6** 10441
[25] Uporov S A, Ryltsev R E, Sidorov V A, Estemirova S K, Sterkhov E V, Balyakin I A and Chtchelkatchev N M 2022 *Intermetallics* **140** 107394
[26] Zhu Q, Xiao G, Cui Y, Yang W, Wu S, Cao G-H and Ren Z 2022 *Scr. Mater.* **210** 114464
[27] von Rohr F, Winiarski M J, Tao J, Klimczuk T and Cava R J 2016 *Proc. Natl. Acad. Sci. U.S.A.* **113** E7144
[28] von Rohr F O and Cava R J 2018 *Phys. Rev. Mater.* **2** 034801
[29] Parizh M, Lvovsky Y and Sumption M 2016 *Supercond. Sci. Technol.* **30** 014007
[30] Liu J, Cheng J and Wang Q 2013 *IEEE Trans. Appl. Supercond.* **23** 34
[31] Zhang J-F, Gao M, Liu K and Lu Z-Y 2020 *Phys. Rev. B* **102** 195140

[32] Hanada S, Nagata A, Den S and Izumi O 1984 *J. Mater. Sci.* **19** 2795
[33] Hutchison T S, Ocampo G and Carpenter G J C 1985 *Scripta Mater.* **19** 635
[34] Guo J, Lin G, Cai S, Xi C, Zhang C, Sun W, Wang Q, Yang K, Li A and Wu Q 2019 *Adv. Mater.* **31** 1807240
[35] Hoffmann N, Cerqueira T F T, Borlido P, Sanna A, Schmidt J and Marques M A L 2023 *npj Comput. Mater.* **9** 1
[36] Rodríguez-Carvajal J 1993 *Phys. B Condens. Matter* **192** 55
[37] Kresse G and Hafner J 1993 *Phys. Rev. B* **47** 558
[38] Kresse G and Furthmüller J 1996 *Phys. Rev. B* **54** 11169
[39] Perdew J P, Burke K and Ernzerhof M 1996 *Phys. Rev. Lett.* **77** 3865
[40] Van De Walle A, Asta M and Ceder G 2002 *Calculation of defect chemistry using the CALPHAD approach, Calphad* **26** 539
[41] Van De Walle A 2009 *Calculation of defect chemistry using the CALPHAD approach, Calphad* **33** 266
[42] He Y, You Y-X, Zeng L, Guo S, Zhou H, Li K, Huang Y, Yu P, Zhang C, Cao C and Luo H 2022 *Phys. Rev. B* **105** 054513
[43] Splett J D, Vecchia D F and Goodrich L F 2011 *J. Res. Natl. Inst. Stand. Technol.* **116** 489
[44] Zeng L, Zhou H, Du H, Zhong R, Guo R, Guo S, Su W, Li K, Zhang C, Yu P and Luo H 2023 *Supercond. Sci. Technol.* **36** 035003
[45] Prozorov R and Kogan V G 2018 *Phys. Rev. Appl.* **10** 014030
[46] Luo H, Xie W, Tao J, Pletikosic I, Valla T, Sahasrabudhe G S, Osterhoudt G, Sutton E, Burch K S and Seibel E M 2016 *Chem. Mater.* **28** 1927
[47] Clogston A M 1962 *Phys. Rev. Lett.* **9** 266
[48] McMillan W L 1968 *Phys. Rev.* **167** 331
[49] Kawabata T, Kawasaki S and Izumi O 1998 *Acta Mater.* **46** 2705
[50] Košuth F, Cedervall J, Ek G, Gabáni S, Pristáš G, Orendáč M, Bačkai J, Onufriienko O, Szabó P and Flachbart K 2024 *Low Temp. Phys.* **50** 663
[51] Li K, Lin W, Guo R, Guo S, Zeng L, Li L, Yu P, Wang K, Zhang C and Luo H 2024 *Mater. Today Commun.* 108444
[52] Kim G, Lee M-H, Yun J H, Rawat P, Jung S-G, Choi W, You T-S, Kim S J and Rhyee J-S 2020 *Acta Mater.* **186** 250
[53] Matthias B T 1955 *Phys. Rev.* **97** 74
[54] Collver M M and Hammond R H 1973 *Phys. Rev. Lett.* **30** 92
[55] Zeng L, Hu X, Zhou Y, Boubeche M, Guo R, Liu Y, Luo S C, Guo S, Li K and Yu P 2024 *Adv. Sci.* **11** 2305054